2nd Advanced Optical Metrology Compendium

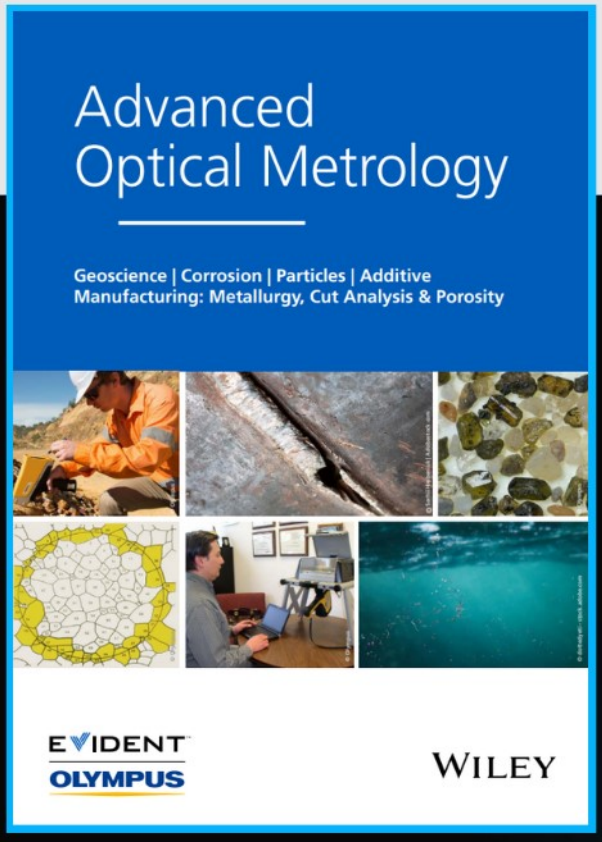

The latest eBook from Advanced Optical Metrology. Download for free.

This compendium includes a collection of optical metrology papers, a repository of teaching materials, and instructions on how to publish scientific achievements.

With the aim of improving communication between fundamental research and industrial applications in the field of optical metrology we have collected and organized existing information and made it more accessible and useful for researchers and practitioners.

EVIDENT
OLYMPUS

WILEY

NANO · MICRO small
www.small-journal.com

High-Performance Photocatalytic Reduction of Nitrogen to Ammonia Driven by Oxygen Vacancy and Ferroelectric Polarization Field of $SrBi_4Ti_4O_{15}$ Nanosheets

Shuai Gao, Haodong Ji, Peng Yang, Ming Guo, John Tressel, Shaowei Chen,* and Qiang Wang**

Photo-responsive semiconductors can facilitate nitrogen activation and ammonia production, but the high recombination rate of photogenerated carriers represents a significant barrier. Ferroelectric photocatalysts show great promise in overcoming this challenge. Herein, by adopting a low-temperature hydrothermal procedure with varying concentrations of glyoxal as the reducing agent, oxygen vacancies (Vo) are effectively produced on the surface of ferroelectric $SrBi_4Ti_4O_{15}$ (SBTO) nanosheets, which leads to a considerable increase in photocatalytic activity toward nitrogen fixation under simulated solar light with an ammonia production rate of 53.41 μmol g^{-1} h^{-1}, without the need of sacrificial agents or photosensitizers. This is ascribed to oxygen vacancies that markedly enhance the self-polarization and internal electric field of ferroelectric SBTO, and hence, facilitate the separation of photogenerated charge carriers and light trapping as well as N_2 adsorption and activation, as compared to pristine SBTO. Consistent results are obtained in theoretical studies. Results from this study highlight the significance of surface oxygen vacancies in enhancing the performance of photocatalytic nitrogen fixation by ferroelectric catalysts.

1. Introduction

Ammonia (NH_3) is a major fertilizer, chemical feedstock, and non-carbon-based energy carrier for hydrogen storage.[1] Nitrogen fixation occurs primarily in nature, where enzymatic reactions in plants and microbes produce 150–200 Tg of ammonia per year.[2] The Haber–Bosch method is an important breakthrough in the history of artificial nitrogen fixation, allowing for a significant increase in NH_3 production.[3] Nonetheless, because of the high stability of N_2 molecules (N≡N bond energy 941.3 kJ mol^{-1}), the conventional Haber–Bosch process is energy- and capital-intensive with substantial environmental impacts, accounting for nearly 2% of global energy consumption and 1% of global greenhouse gas emissions.[4] Photocatalytic nitrogen fixation has been attracting extensive interest due to its mild, low-energy, and environmentally benign reaction conditions.[5]

Thus far, a variety of semiconductor materials, in particular those with excellent visible light absorption, have been developed for photocatalytic ammonia synthesis; yet, the inefficient separation of photogenerated carriers has severely limited the performance.[6] In recent studies, piezoelectric materials have emerged as a viable candidate as they can produce a polarization-induced electric field by the displacement of the positive and negative charge centers onto opposite sides, and the resultant internal electric field (IEF) can significantly impede the recombination of photogenerated electron–hole pairs.[7] For instance, piezoelectric photocatalysts with a ferroelectric tetragonal $BaTiO_3$@C core–shell structure have been found to effectively degrade organic pollutants.[8] In another study,[9] the CO_2 photoreduction efficiency is drastically increased by the polarization-induced electric field of corona-polarized ferroelectric Bi_3TiNbO_9.

As a layered bismuth-based material,[10] ferroelectric $SrBi_4Ti_4O_{15}$ (SBTO) possesses a high Curie temperature (520 °C), can maintain a stable ferroelectric phase at room temperature,[11] and is known to exhibit self-polarization, which originates from the $[TiO_6]$ octahedral distortion, with the polarization direction parallel to the $[Bi_2O_2]^{2+}$ layer.[12] The resultant

S. Gao, M. Guo, Q. Wang
Laboratory for Micro-sized Functional Materials and College of Elementary Education and Department of Chemistry
Capital Normal University
Beijing 100048, P. R. China
E-mail: qwchem@gmail.com

H. Ji
School of Environment and Energy
Peking University Shenzhen Graduate School
Shenzhen 518055, P. R. China
E-mail: jihaodong@pku.edu.cn

P. Yang
Key Laboratory of Synthetic and Natural Functional Molecule Chemistry
College of Chemistry and Materials Science
Northwest University
1 Xuefu Ave., Xi'an 710127, P. R. China

J. Tressel, S. Chen
Department of Chemistry and Biochemistry
University of California
1156 High Street, Santa Cruz, CA 95064, USA
E-mail: shaowei@ucsc.edu

The ORCID identification number(s) for the author(s) of this article can be found under https://doi.org/10.1002/smll.202206114.

DOI: 10.1002/smll.202206114

IEF can facilitate the separation of photogenerated carriers, which has been demonstrated recently in the dramatically increased efficiency of CO_2 photoreduction.[13] Yet, studies on the application of SBTO photocatalysts for nitrogen fixation have remained scarce thus far. One major hurdle in nitrogen photoreduction is the limited interaction between the photocatalysts and N_2 molecules, and defect engineering has been recognized as an effective strategy.[14] Oxygen vacancies (Vo), the most commonly found defects, have indeed been shown to cause a variation of the color appearance, optical absorption, and electrochemical properties of the photocatalysts, and more importantly, serve as the favorable reaction sites for promoting the adsorption and activation of reactant molecules.[15] For instance, we observed that the formation of oxygen vacancies boosted the kinetics of N_2 photoreduction to NH_3 by Bi_5O_7Br nanotubes.[16] Mechanistically, this was accounted for by oxygen vacancies that facilitated the chemisorption of inert nitrogen molecules (Vo−N=N), elongated the N≡N bond, and promoted N≡N activation. Therefore, it is of both fundamental and technological significance to optimize the photocatalytic performance of SBTO toward N_2 photoreduction within the context of surface oxygen vacancies and self-polarization. This is the primary motivation of the present study.

The formation of oxygen vacancies in photocatalysts is typically driven by thermal treatment at elevated temperatures in vacuum or in a controlled atmosphere (e.g., H_2, N_2, Ar), which usually requires stringent conditions, poses certain safety hazards, and is uneconomical in industrial applications.[17] Development of effective alternatives is strongly desired. In the present study, glyoxal (OCHCHO, the smallest dialdehyde), a classical mild reducing agent, was used to induce the formation of oxygen vacancies on the surface of ferroelectric SBTO by a two-step, low-temperature hydrothermal procedure.[9,17b,18] The resultant sample (exhibited a maximum N_2 to NH_3 fixation efficiency of 53.41 μmol g^{-1} h^{-1} under simulated sunlight. Results from the experimental studies and density functional theory (DFT) calculations suggested that oxygen vacancies and ferroelectric polarization fields synergistically facilitated the nitrogen adsorption, activation, and reduction due to the formation of three electron-transfer pathways that increased the separation efficiency; and hence, concentration of photogenerated carriers.

2. Results and Discussion

2.1. Sample Preparation and Structural Characterizations

Scheme 1 depicts the procedure for the preparation of oxygen vacancy-enriched SBTO (Vo-SBTO) nanosheets, which consist of two major steps. SBTO was first prepared by a hydrothermal treatment of tetrabutyl titanate, bismuth nitrate, and strontium chloride at 180 °C for 24 h. To produce oxygen vacancies on the SBTO surface, the SBTO powders were mixed with an aqueous solution of glyoxal at different concentrations (i.e., 0, 0.03, 0.15, and 0.3 M) before being subject to a second hydrothermal treatment at 120 °C for 5 h. The corresponding samples were referred to as SBTO, SBTO-1, SBTO-2, and SBTO-3, respectively. The experimental details are included in the Supporting Information.

SBTO exhibits a classic Aurivillius-type crystal structure consisting of $[Bi_2O_2]^{2+}$ layers and staggered $[TiO_6]$ octahedra, with Sr and Bi atoms co-occupying the inner area of the $[TiO_6]$ octahedron (**Figure 1**a). It can crystallize into the polar non-centrosymmetric orthorhombic space group A21am with lattice parameters of a = 5.45070 Å, b = 5.43760 Å, and c = 40.98410 Å.[19] Inside the crystal, this arrangement produces charge separation fields.[12,13] Figure 1b shows the X-ray diffraction (XRD) patterns of the pristine SBTO nanosheets and Vo-SBTO prepared at different glyoxal concentrations, where the Bragg diffraction peaks at 2θ = 23.26°, 30.43°, 32.90°, 39.76°, 47.28°, and 57.32° can be assigned to the (111), (119), (020), (0210), (220), and (319) planes, respectively, consistent with those of the orthorhombic phase SBTO (A21am, PDF-#43-0973). Notably, no other peaks are found, suggesting high purity of the samples and the formation of oxygen vacancies do not alter the crystalline phase of SBTO.

The sample structures were then characterized by scanning electron microscopy (SEM) and transmission electron microscopy (TEM) measurements. From Figure 1c and Figures S1 and S2 (Supporting Information), SBTO could be found to consist of stacks of nanosheets, and the morphology remained largely unchanged after low-temperature hydrothermal treatment for Vo formation. Atomic force microscopy (AFM) topographic measurements show that the SBTO samples indeed exhibited a nanosheet morphology with a thickness ≈20 nm, which was equivalent to five unit-cell layers (Figure S3, Supporting Information). Elemental mapping analysis based on energy-dispersive X-ray (EDX) spectroscopy shows a homogeneous distribution of the Sr, Bi, Ti, and O elements within the sample (Figure 1d). In high-resolution TEM measurements (Figure 1e,f), well-defined lattice fringes can be readily observed in SBTO-2 with an interplanar distance of 0.273 nm, corresponding to the (020) planes of SBTO (PDF-#43-0973). The corresponding selected area electron diffraction (SAED) patterns show that the main exposed facet was the crystal plane along the *c*-axis (Figure 1g), and these SBTO nanosheets were grown along the {001} direction (Figure S4, Supporting Information). In addition, one could see the formation of an amorphous (defective) layer (≈1.5 nm) at the edge of the SBTO-2 nanosheets (Figure 1e), which was absent in SBTO (Figure S5, Supporting Information).

Consistent results were obtained in Raman measurements (Figure S6, Supporting Information), where the energy of the stretching vibration of the $[TiO_6]$ octahedron[11,20] increased in the order of SBTO (259.82 cm^{-1}) < SBTO-1 (264.74 cm^{-1}) < SBTO-2 (271.90 cm^{-1}) < SBTO-3 (277.44 cm^{-1}), most likely due to a change of the Ti coordination environment, where partial oxygen loss caused lattice distortion in the $[TiO_6]$ octahedra. Nitrogen sorption measurements show that the Brunauer–Emmett–Teller (BET) specific surface area and average pore size increased markedly with hydrothermal treatments with an increasing amount of glyoxal, SBTO (79.26 m^2 g^{-1}, 0.29 nm) < SBTO-1 (96.23 m^2 g^{-1}, 0.28 nm) < SBTO-2 (330.51 m^2 g^{-1}, 0.45 nm) < SBTO-3 (340.20 m^2 g^{-1}, 0.48 nm), whereas an opposite trend was observed with the average pore volume, SBTO (14.61 cm^3 g^{-1}) > SBTO-1 (11.73 cm^3 g^{-1}) > SBTO-2 (5.45 cm^3 g^{-1}) ≈ SBTO-3 (5.58 cm^3 g^{-1}) (Figure S7 and Table S1, Supporting Information). This can be accounted for by the formation of an amorphous (defective) layer on the Vo-SBTO surface which was facilitated by glyoxal reduction (Figure 1e).

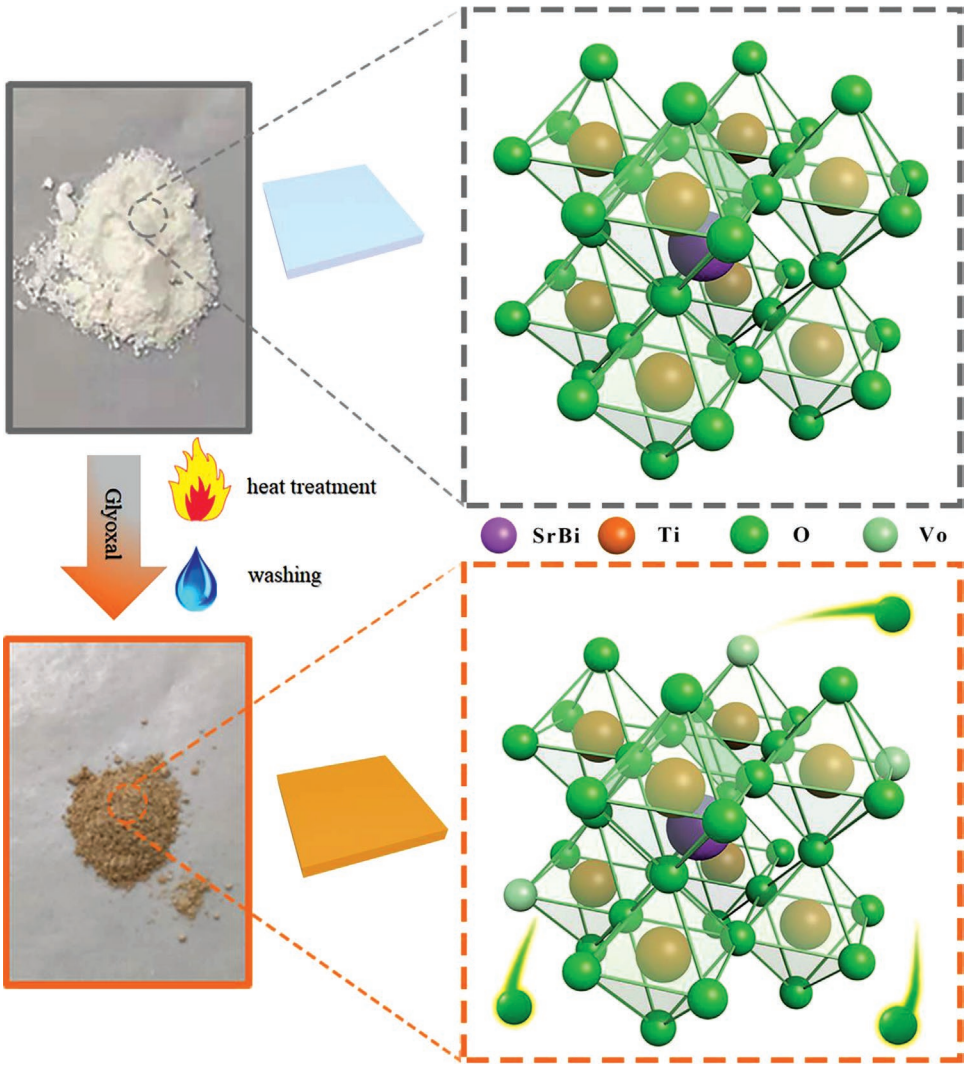

Scheme 1. Schematic illustration of the preparation of oxygen vacancy-enriched SBTO nanosheets.

X-ray photoelectron spectroscopy (XPS) measurements were then performed to investigate the chemical composition and valency of the samples. From the survey spectra in Figure S8 (Supporting Information), the elements of Sr, Bi, Ti, and O can be readily identified in all samples at ≈159.1, 163.6, 457.8, and 529.5 eV, respectively. **Figure 2**a shows the high-resolution scans of the Bi 4f and Sr 3d electrons, where the binding energies of the Bi(III) 4f doublet can be found at 158.1/163.4 eV and the Sr(II) 3d doublet at 131.8/133.5 eV for all samples in the series,[13,18b] suggesting that oxygen vacancies were unlikely to form in the $[Bi_2O_2]^{2+}$ layer. In the corresponding Ti 2p scans (Figure 2b), SBTO can be found to exhibit two peaks at 458.1 and 463.93 eV, due to the $2p_{3/2}$ and $2p_{1/2}$ electrons of Ti(IV) (the other peak at 465 eV is due to Bi $4d_{3/2}$);[21] whereas for the Vo-SBTO samples, the Ti $2p_{3/2}$ binding energy decreases rather substantially to 458.04 eV for SBTO-1, 457.98 eV for SBTO-2, and 457.92 eV for SBTO-3, in good agreement with results from Raman measurements that oxygen vacancies were most likely formed in the $[TiO_6]$ octahedra.[22] Deconvolution of the O 1s spectra (Figure 2c) yielded two peaks at 529.7 and 531.2 eV for all samples, which could be indexed to lattice oxygen and surface hydroxyl, respectively.[18b,23] An additional O 1s peak could be deconvoluted at 532.5 eV for the three Vo-SBTO samples, due to adsorbed H_2O molecules.[24] This suggests that the adsorption of H_2O is facilitated by oxygen vacancies, consistent with water contact angle measurements (Figure S9, Supporting Information). Note that enhanced hydrophilicity is conducive to N_2 adsorption in solution (Figure S10, Supporting Information).

X-ray absorption spectroscopy (XAS) measurements were then carried out to further reveal the atomic arrangements and defect configurations of the samples. The normalized Ti K-edge XAS profiles are shown in Figure 2d. One can see that there was no significant change of the overall spectral features between SBTO and SBTO-2, suggesting good retention of the SBTO crystal phase, despite the formation of Vo after hydrothermal reduction with glyoxal. In addition, the absorption edge energies of SBTO and SBTO-2 are very consistent with that of the TiO_2 reference, but markedly different from that of Ti foil, in agreement with the Ti(IV) valence state as determined in XPS measurements. Furthermore, one may notice a small red-shift

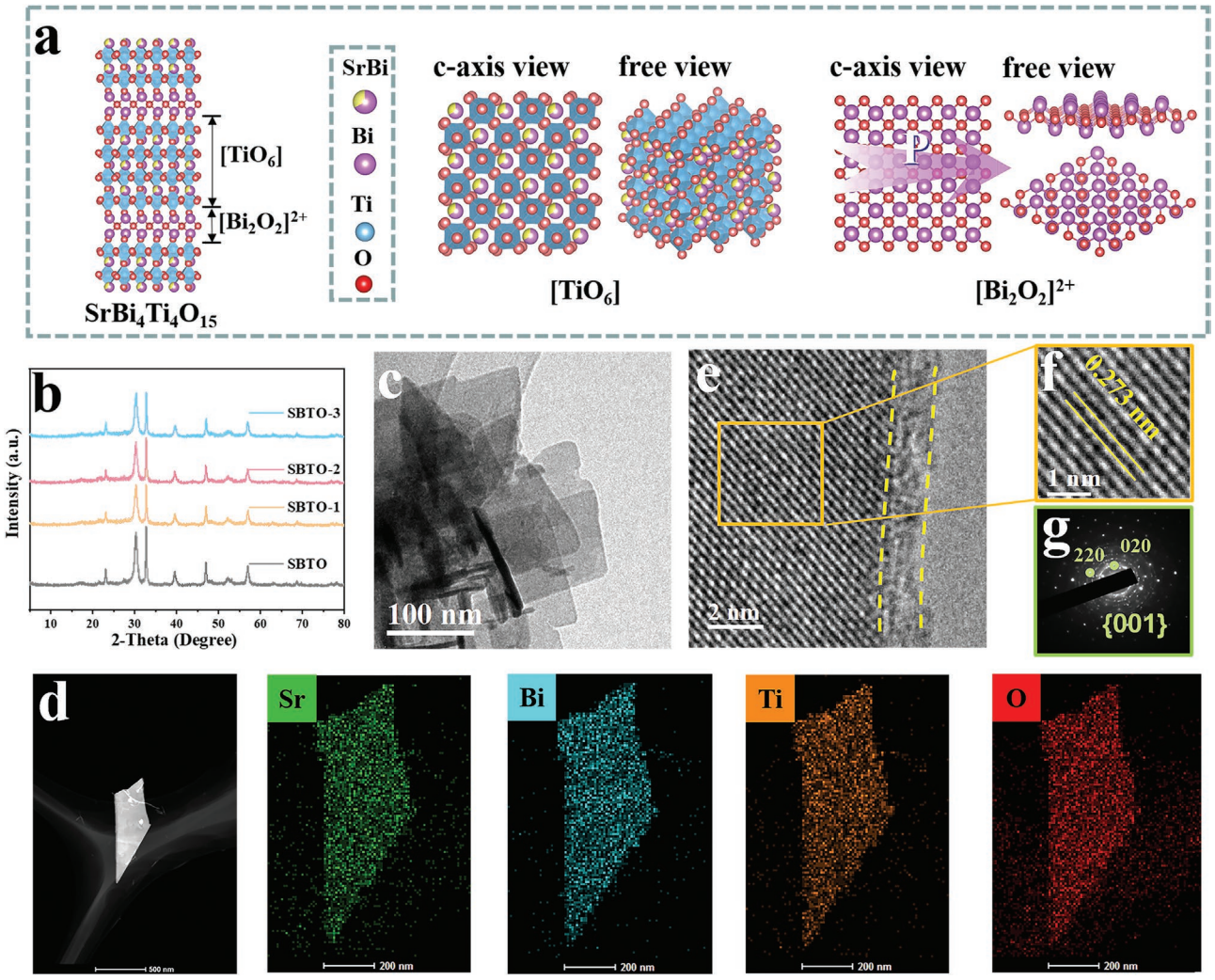

Figure 1. a) Crystal structure of SBTO. b) XRD patterns of SBTO, SBTO-1, SBTO-2, and SBTO-3. c,e,f) TEM images, d) EDX-based elemental maps, and g) SAED patterns of SBTO-2.

of the Ti K edge of SBTO-2 (4985.72 eV), as compared to that of pristine SBTO (4985.93 eV), along with a somewhat diminished white line peak intensity, consistent with the formation of Vo and a slightly decreased valence state of Ti. The Fourier transforms (FT) of the Ti K-edge extended X-ray absorption fine structure (EXAFS) profiles are shown in Figure 2e, where SBTO can be seen to display a prominent peak at 1.48 Å for the Ti—O path, and this peak is somewhat weakened and shifted to a lower value of 1.44 Å for SBTO-2, whereas for TiO_2, the Ti—O path appears at a somewhat larger R value of 1.53 Å, and Ti foil exhibits only a single peak at 2.52 Å for Ti—Ti. This discrepancy of atomic arrangements can also be visualized in the EXAFS wavelet transforms in Figure 2f, where the Ti—O path can be found at 5.05 $Å^{-1}$ for SBTO and 5.04 $Å^{-1}$ for SBTO-2, in comparison to 5.69 $Å^{-1}$ for TiO_2, whereas the Ti—Ti path can be found at 6.38 $Å^{-1}$ for Ti foil.

Electron paramagnetic resonance (EPR) measurements were then carried out to probe the formation of oxygen vacancies.[3b,25] There are three possible oxygen vacancies: Bi—Vo—Bi, Ti—Vo—Bi, and Ti—Vo (Figure 2g). DFT calculations showed that the formation energies were ≈ –0.2698 eV for Ti—Vo, –0.7582 eV for Ti—Vo—Bi, and –0.3477 eV for Bi—Vo—Bi (Figure 2h), suggesting that Ti—Vo—Bi oxygen vacancies are energetically preferred, consistent with their formation within the [TiO_6] octahedra (inset to Figure 2h), as suggested in the above XPS and Raman measurements. This is indeed manifested in EPR measurements. From Figure 2i, one can see that in contrast to the featureless profile of SBTO, the three Vo-SBTO samples all exhibited a well-defined signal at g = 2.004 that is consistent with oxygen vacancy, and the peak-to-peak intensity increased in the order of SBTO-1 < SBTO-2 < SBTO-3.[26] Taken together, these results indicate that oxygen vacancies could be readily produced within the [TiO_6] octahedra of SBTO nanosheets by low-temperature hydrothermal treatment with glyoxal, and the concentration increased with an increasing loading of the reducing agent.

In fact, in contrast to the white appearance of SBTO, the Vo-SBTO samples all exhibited a brown color which became increasingly darkened from SBTO-1 to SBTO-2 and SBTO-3 (Figure S11, Supporting Information). This is likely due to

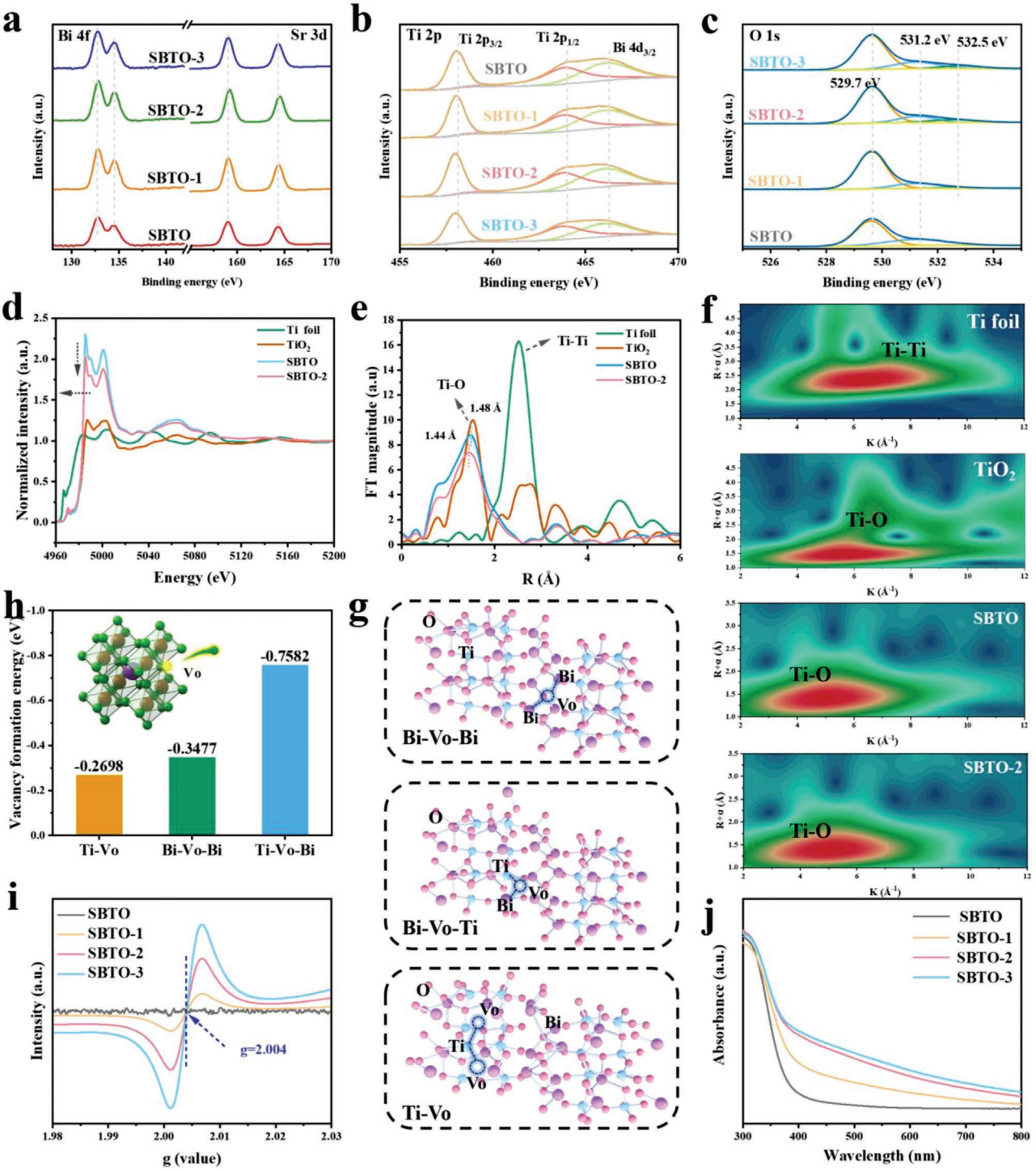

Figure 2. XPS spectra of the a) Bi 4f and Sr 3d, b) Ti 2p, and c) O 1s electrons of pristine SBTO and Vo-SBTO. d) Normalized Ti K edge XAFS spectra and e) the k^3-weighted Fourier transforms of the EXAFS spectra of the Ti coordination environment for pristine SBTO and SBTO-2. f) Wavelet transforms (WT) of SBTO and SBTO-2. g) Three oxygen-vacancy models for DFT theoretical calculations and h) their corresponding vacancy formation energies (with the oxygen vacancy configuration shown in the panel inset). i) EPR Spectra and j) UV–vis diffuse reflectance spectra (DRS) of the SBTO sample series.

plasma resonance of surface-trapped electrons in oxygen vacancies. The optical properties of SBTO and Vo-SBTO were then examined by UV–vis diffuse reflectance spectroscopy (DRS) measurements (Figure 2j). SBTO exhibited an absorption edge at ≈397 nm, corresponding to a band gap of ≈3.0 eV.[13] By contrast, the Vo-SBTO samples all displayed apparent absorption even in the visible range (400–700 nm), and from the Tauc plots in Figure S12, Supporting Information, the forbidden band

gap was found to be markedly lower, decreasing in the order of SBTO-1 (2.60 eV) > SBTO-2 (2.40 eV) > SBTO-3 (2.28 eV), consistent with the increasing concentration of oxygen vacancies. Furthermore, from the Mott–Schottky analysis (Figure S13, Supporting Information), the energy of the conduction band (CB) was estimated to be –1.73 eV for SBTO, –1.33 eV for SBTO-1, –1.17 eV for SBTO-2, and –0.93 eV for SBTO-3, downshifting with increasing oxygen vacancy concentration.

2.2. Photocatalytic Reduction of Nitrogen

The performance in photocatalytic nitrogen fixation was then assessed by dispersing the samples in ultrapure water without any sacrificial agents using a 300 W xenon lamp as the light source. All reactions were carried out at 25 °C under continuous light irradiation for 4 h. NH_4^+ was detected and quantified by the Nessler's reagent method against the calibration curves in Figure S14 and Tables S2–S6 (Supporting Information).[27] From **Figure 3**a and Figure S15 (Supporting Information), one can see that SBTO exhibited only a minimal activity, and the performance was markedly enhanced with Vo-SBTO, signifying the importance of oxygen vacancies in N_2 activation and reduction. Among the series, SBTO-2 exhibited the best photocatalytic performance, producing 179.21 μmol g^{-1} of NH_3 in 4 h with an NH_3 production rate of 53.41 μmol g^{-1} h^{-1}. This is likely because too high an oxygen vacancy concentration might lead to trapping of charge carriers; and hence, a reduced photocatalytic performance (the NH_3 production rate decreased to 18.96 μmol g^{-1} h^{-1} for SBTO-3).[28] Note that the performance of SBTO-2 is highly comparable to leading results reported recently in the literature with relevant catalysts (Table S7, Supporting Information).

Notably, ion chromatography measurements showed a very consistent yield of NH_3 production after 4 h's reaction at 197.33 μmol g^{-1} on SBTO-2 (Figure S16, Supporting Information), and the apparent quantum yield (AQY) was found to decrease with photoirradiation at increasing wavelength, at 0.9% and 0.63% under monochromatic light at 365 and 420 nm, respectively. O_2 was also detected by gas chromatography analysis due to water oxidation (which also produced protons for NH_3 synthesis) (Figure 3b; inset of Tables S8 and S9, Supporting Information); and no other by-products such as N_2H_4 were identified (Figures S17 and S18 and Table S10, Supporting Information), demonstrating excellent selectivity of the SBTO photocatalysts in nitrogen fixation to NH_3.

Notably, to minimize catalyst contamination, all samples were rinsed three times with ultrapure water to remove N-containing contaminants adsorbed on the surface before being placed in the reactor (Figure S19, Supporting Information).[29] Furthermore, the fact that no NH_4^+ was produced in the dark without the photocatalyst or under Ar purging (Figure S20, Supporting Information) indicates that the SBTO samples were free of nitrogen contamination. In addition, the interference of human respiration and ammonia in air was largely negligible (Figure S21, Supporting Information). To confirm that N_2 was the sole source of conversion to NH_3, isotopic labeling was also performed using $^{14}N_2$ and $^{15}N_2$ as the feed gases, and the products were analyzed by ^{1}H NMR spectroscopy (Figure 3c). When $^{15}N_2$ was bubbled into the reactor, only the $^{15}NH_4^+$ signal (a doublet) was observed, whereas with $^{14}N_2$ as the feed gas, only $^{14}NH_4^+$ (a triplet) was detected, indicating that N_2 was indeed produced from the feed gases and not from other contaminants. In addition, the SBTO catalysts exhibited excellent stability and reusability. After four cycles of experiments, the ammonia yield remained virtually unchanged (Figure S22, Supporting Information), and no appreciable change of the SBTO-2 materials structure was detected in XRD, TEM, EPR, and XPS measurements (Figures S23–S26, Supporting Information).

Consistent results were obtained in photoelectrochemical measurements. Under the irradiation of simulated solar light, SBTO-2 exhibited the greatest photocurrents among the sample series (Figure S27, Supporting Information), suggesting the highest efficiency of charge separation. This is in excellent agreement with results from photoluminescence (PL) measurements, where the emission intensity decreased in the order of SBTO > SBTO-1 > SBTO-3 > SBTO-2 (Figure S28, Supporting Information). The time-resolved transient luminescence decay profiles are depicted in Figure S29 and Table S11, Supporting Information, where the average lifetime was estimated to be 2.92 ns for pristine SBTO and 6.72 ns for SBTO-2, suggesting a markedly higher charge separation efficiency for the latter. In electrochemical impedance (EIS) measurements (Figure S30, Supporting Information), SBTO-2 also possessed the smallest charge-transfer resistance (R_{CT}) among the sample series.

The carrier density (N_d) of the sample was then calculated from the slope of the Mott–Schotty plot by using the following equation,[30] $N_d = \frac{2}{e_0 \varepsilon \varepsilon_0}\left[\frac{d\left(\frac{1}{C^2}\right)}{dV}\right]^{-1}$, where e_0 is the electron charge (1.6×10^{-19} C), ε is the dielectric constant of SBTO (ε = 220 F m^{-1}),[31] ε_0 is the vacuum dielectric constant (8.86×10^{-12} F m^{-1}), and V is the applied bias at the electrode. Among the sample series, SBTO-2 can be seen to exhibit the highest carrier density, pristine SBTO (3.10×10^{17}) < SBTO-1 (3.21×10^{18}) < SBTO-3 (3.33×10^{18}) < SBTO-2 (5.14×10^{18}).

The nature of N_2 adsorption on SBTO and Vo-SBTO surfaces was then investigated by temperature-programmed nitrogen (N_2-TPD) desorption measurements (Figure 3d). For SBTO, a single desorption peak started to appear at 81 °C and centered at 137 °C, which was attributed to physisorbed N_2;[32] by contrast, N_2 desorption from SBTO-2 commenced at a much higher temperature (≈250 °C), featuring two peaks at 373.74 °C and 529.72 °C, due to chemisorbed N_2 on the sample surface.[32b] This suggests that surface defects (oxygen vacancies) facilitated the chemisorption of N_2 molecules, a critical step in the activation and ultimately reduction of N_2.[33]

The adsorption and activation of N_2 molecules on the surface of SBTO-2 were then probed by in situ Fourier-transform infrared (FTIR) spectroscopy measurements. From Figure 3e, it can be seen that in the dark, the vibrational peak at 1624 cm^{-1} of chemisorbed N_2 molecules on the sample surface (Vo—N=N) became intensified with increasing adsorption time (up to 20 min).[34] This confirms that Vo can promote the chemisorption of N_2 molecules on the catalyst surface. Upon the exposure to simulated sunlight, a range of new vibrational bands emerged (Figure 3f): NH_4^+ vibrations at 1363, 1403, 1460,

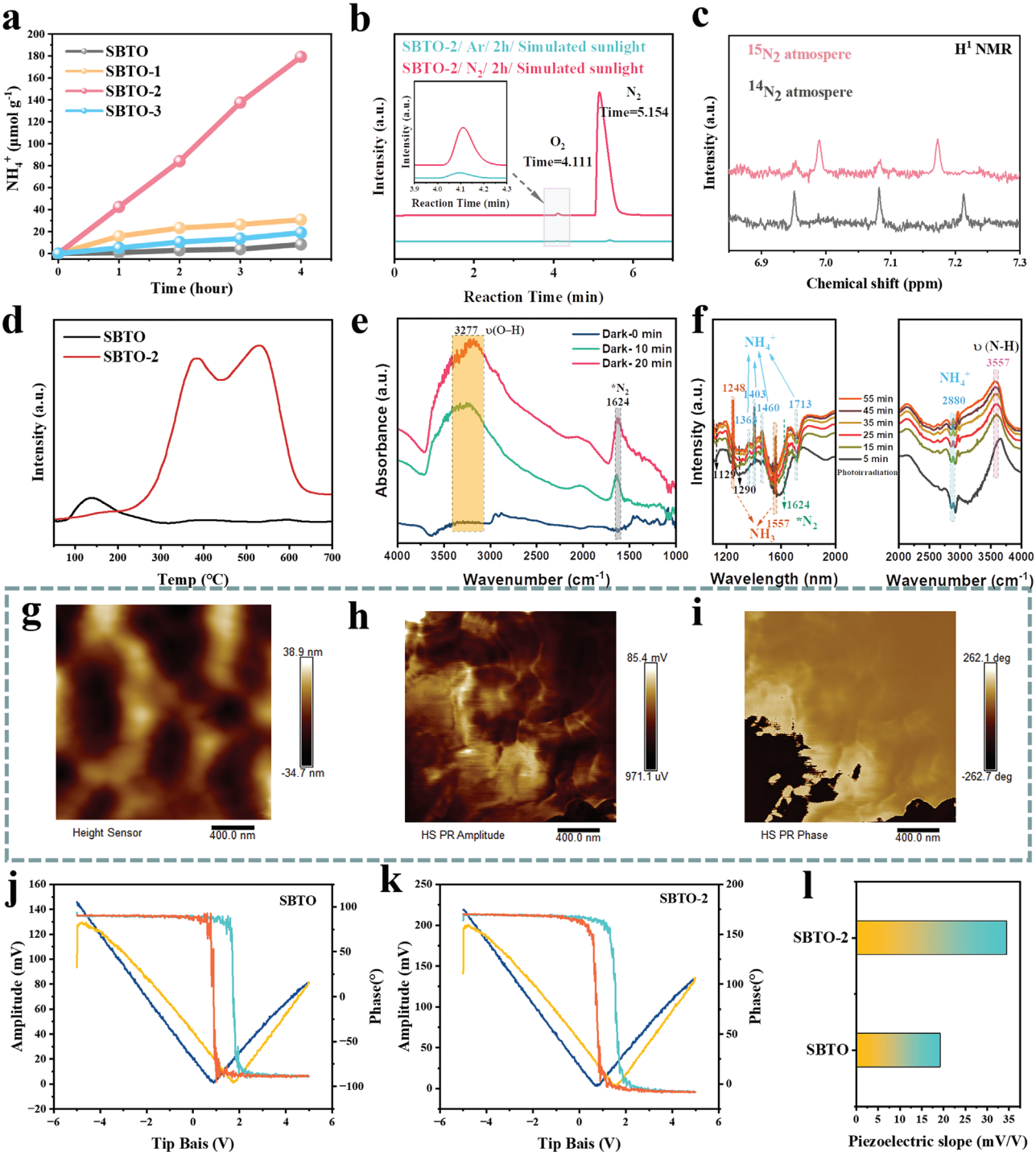

Figure 3. a) Photocatalytic NH_3 Synthesis by SBTO and Vo-SBTO under simulated sunlight for different irradiation times. b) Detection of gaseous products (H_2 and O_2) by gas chromatography. Inset is the zoom in of the box area. c) ^{1}H NMR spectra of $^{14}NH_3/^{14}NH_4^+$ and $^{15}NH_3/^{15}NH_4^+$ catalyzed by SBTO-2 using ^{14}N or ^{15}N as the N_2 sources. d) N_2-TPD curves of SBTO and SBTO-2. In situ FTIR spectra of SBTO-2 e) in the dark and f) under photoirradiation for up to 55 min. g) PFM topograph, h) amplitude, and i) phase mapping of SBTO-2. Phase curves and butterfly amplitude loops of j) SBTO and k) SBTO-2. l) Slopes of the hysteresis loops of SBTO and SBTO-2 in panels (j,k).

1713, and 2880 cm^{-1},[35] vibrations of NH_3 molecules adsorbed on the catalyst surface at 1248 and 1557 cm^{-1},[3b] ν(N—H) at 3557 cm^{-1},[16] and σ(O—H) at 1320 cm^{-1}.[33b] The intensity increased gradually with the prolongation of light irradiation, indicating the promoting effect of Vo on the conversion of N_2 molecules to NH_4^+. Notably, the characteristic vibrations of N_2H_4 at 1129 and 1290 cm^{-1} were not observed,[35a] which is consistent with the absence of N_2H_4 by chromogenic detection.

These findings provide strong evidence for a possible distal nitrogen fixation pathway.

The influence of oxygen vacancies on the SBTO ferroelectric properties was then analyzed. From Figure S31 (Supporting Information), one can see that Vo-SBTO exhibited a markedly higher remanent polarization (P_r) than SBTO. This can be accounted for by the oxygen vacancies that formed defective dipoles in the presence of an applied electric field, thereby generating a locally built-up electric field. Electric fields produced in the close proximity to ferroelectric domain barriers may limit domain switching.[9,36]

Piezoelectric force microscopy (PFM) measurements were then performed to verify the actual piezoelectric properties of the samples. The morphology, amplitude, and phase images of SBTO-2 and SBTO are shown in Figure 3g–i and Figure S32 (Supporting Information), respectively. When the PFM conductive tip was scanned over the SBTO and SBTO-2 surfaces, the comparison of phase and amplitude images signified the presence of randomly distributed ferroelectric domains, and the bright and dark regions indicated different deflection directions. The signaturatory butterfly amplitude loop and phase curve demonstrate the typical piezoelectric characteristics of SBTO and SBTO-2 when a tip bais of ±5 V was applied to the sample surface (Figure 3j,k). A segment in the amplitude-voltage loop was selected, and then, the length of the horizontal coordinate was divided by the vertical coordinate as a measure of the piezoelectric intensity of the sample (Figure 3l).[37] It can be seen that the introduction of Vo significantly enhanced the piezoelectric response of the SBTO.

Furthermore, photo-assisted Kelvin probe force microscopy (KPFM) measurements were conducted to examine the migration behaviors of photogenerated charges. AFM topographic measurements showed virtually no change of the sample morphologies before and after photo illumination (**Figure 4**a; Figure S33, Supporting Information). The average surface potential of SBTO was estimated to be 173.62 mV in the dark and decreased to 160.82 mV under photoirradiation and to 163.08 mV when the light was turned off (Figures S34 and S35, Supporting Information). For Vo-SBTO, the average surface potential was markedly higher (Figure 4b–f), 423.75 mV in the dark, 359.28 mV under photoirradiation, and 379.07 mV with the light turned off. The diminishment of the surface potential under the photoirradiation can be ascribed to the charge shielding effect arising from the accumulation of photogenerated holes and electrons on the opposite sites of the ferroelectric materials.[38] Such a charge–transfer ability is represented by the surface potential difference ($\Delta\Phi$) between that in the dark and under photoirradiation,[36a,38,39] which was 12.8 mV for SBTO and 64.47 mV for SBTO-2, suggesting that the formation of oxygen vacancies in Vo-SBTO produced an enhanced surface electric field; and hence, facilitated efficient migration of photogenerated carriers. Notably, after the photo illumination was turned off, the surface potential of Vo-SBTO and SBTO did not return to the pre-illumination level and shifted slightly upward. This may be attributed

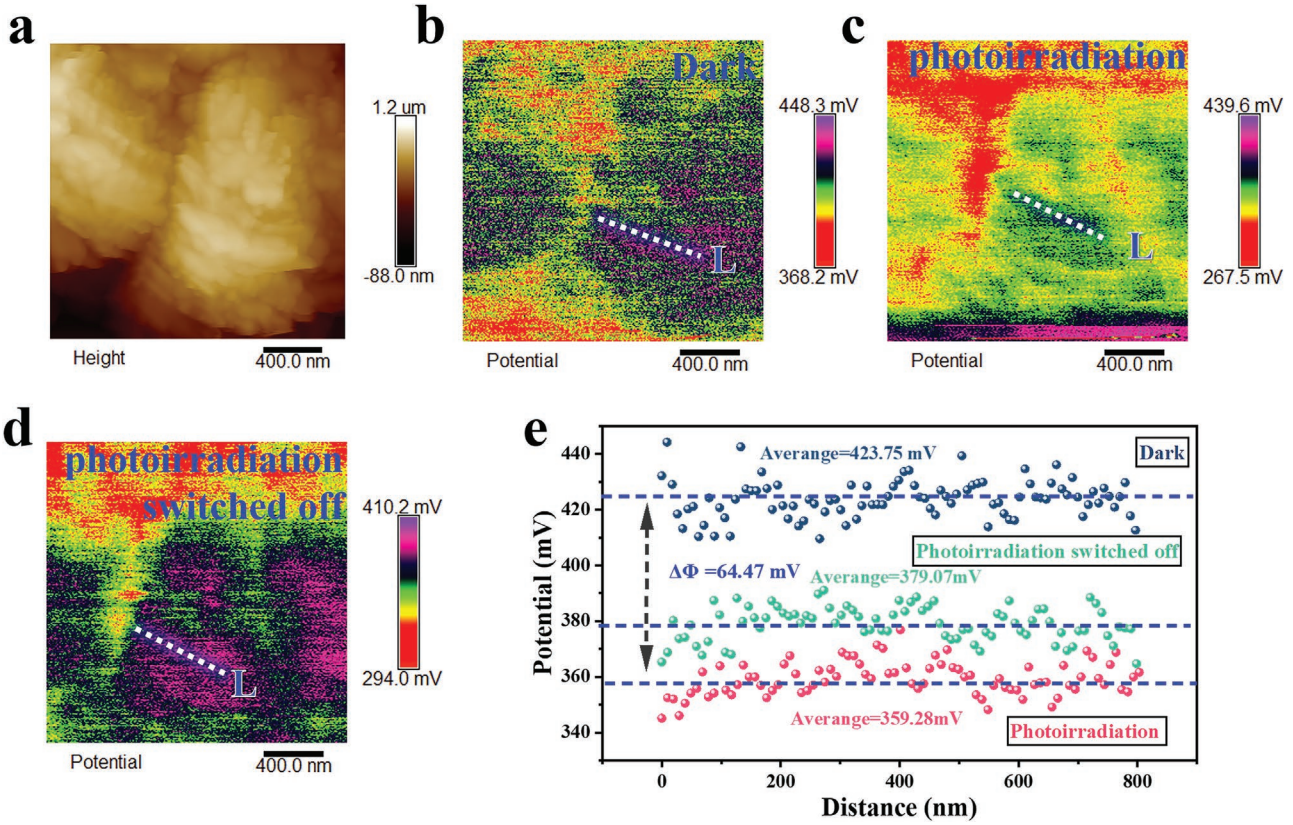

Figure 4. a) AFM topograph of SBTO-2 in the dark. KPFM images of SBTO-2 b) in the dark, c) under photoirradiation, and d) with the photoirradiation switched off. e) The corresponding surface potential distributions along the dashed lines (L) in panels (b–d).

to the suppressed recombination of photogenerated carriers by the IEF and oxygen vacancies. For SBTO, the IEF generated by self-polarization is the main driving force to impede the recombination of photogenerated carriers, whereas in Vo-SBTO, the oxygen vacancies may act as traps of photogenerated electrons and inhibit the indirect complexation of carriers, and the high residual polarization enhances the IEF and inhibits the direct complexation of photogenerated charges. Taken together, these results suggest synergistic interactions of oxygen vacancies and ferroelectric polarization fields in facilitating the migration and separation of photogenerated carriers; and hence, the photocatalytic performance.

To demonstrate the charge transfer pathway of SBTO nanosheets, methanol was used as a sacrificial agent for photogenerated holes, and Pt^{6+} in the reaction solution was reduced by photogenerated electrons.[40] Using IO^{3-} as an electron scavenger, Mn^{2+} in the reaction solution was oxidized to MnO_x by photogenerated holes. In comparison with pristine SBTO, aggregates of small Pt nanoparticles and MnO_x nanoparticles were formed on the surface of SBTO crystals (Figure S36, Supporting Information). This indicates that the photo-excited electrons and holes migrated to two opposite directions under the action of the IFE and underwent reduction–oxidation reactions in the positive or negative polarized regions on the upper and lower sides of the nanosheets. This is consistent with the results observed by KPFM. Notably, the internal polarization of SBTO originates from $[TiO_6]$ distortion, and the polarization direction is parallel to the $[Bi_2O_2]^{2+}$ layer (perpendicular to the [001] growth axis). This means that IEF has the same direction, which is consistent with the results obtained by the photo-deposition experiment (Figure S36c, Supporting Information).

2.3. Theoretical Computation

DFT calculations were then carried out to probe the N_2 to NH_3 mechanism. Two structural models were constructed, pristine SBTO and Vo-SBTO (**Figure 5**a). From the calculated density of states (DOS) of the orbital occupancy of each atom in SBTO, one can see that that CB is mainly composed of Ti 3d and valence band (VB) of the hybridization of O 2p and Bi 6s orbitals (Figures S37 and S38, Supporting Information). The transfer of photogenerated electrons to the $[TiO_6]$ layer will activate (weaken) the N≡N bond. A narrower energy level is observed for Vo-SBTO than for perfect SBTO, and the bottom of the CB appears to shift downward, which is consistent with the experimental results obtained in the above DRS and Mott–Schottky measurements.

The adsorption and protonation of N_2 molecules on the surfaces of perfect SBTO and Vo-SBTO were then simulated and compared, which involves two main mechanisms, dissociative and associative (Figure S39, Supporting Information).[15,33b,41] In the dissociative mechanism, the N≡N bonds are broken before the hydrogenation step, which is energy-costly and not typical in photocatalytic ammonia production. The associative mechanism is generally divided into the distal pathway and the alternating pathway.[16,42] Note that the intermediate steps in the alternating pathway show a high probability of generating N_2H_4. However, as no N_2H_4 was detected in the present study, we would focus on the distal pathway for both pristine SBTO and Vo-SBTO. The structural models and Gibbs free energy diagrams of the intermediates produced during N_2 fixation to NH_3 are shown in Figure 5b,c and Figure S40 (Supporting Information). From Figure 5b and insets to Figure 5c, it can be seen that chemisorption of N_2 is energetically unfavored on the pristine SBTO surface, which is consistent with the N_2-TPD results. By contrast, N_2 molecules can be readily adsorbed on the Ti atoms with unsaturated coordination on the surface of Vo-SBTO and form relatively stable chemical bonds. In fact, the N_2 adsorption energy is higher on Vo-SBTO (–0.577 eV) than on pristine SBTO (–0.535 eV) (Figure S41, Supporting Information). In N_2 reduction to NH_3, the first hydrogenation step is the protonation of $*N_2$ to *N−NH ($*N_2 + H^+ \rightarrow$ *N−NH), which is a potential limiting step in the overall N_2 fixation process.[43] This requires an input energy of 1.22 eV on pristine SBTO but is actually exothermic on Vo-SBTO (–0.585 eV). In the subsequent *N−NH_2 hydrogenation step, a reaction energy barrier of 5.315 eV must be overcome on pristine SBTO, which diminishes markedly to only 0.032 eV on Vo-SBTO. In the subsequent step of the desorption of *N−NH_3 to N* (*N−NH_3→*N), an uphill free energy of 1.829 eV is required, which is most likely the rate-determining step in the entire N_2 reduction process on Vo-SBTO. Notably, although this process is endothermic, the protonation of $*NH_3$ to NH_4^+ in solution is a favorable step.[44] By contrast, this step is exothermic on pristine SBTO. The same phenomenon is observed in the $*NH_3$ desorption on the material surface to produce NH_3(g) ($*NH_3 \rightarrow NH_3$(g)). After the largest thermodynamic energy barrier, the subsequent protonation from *N is exothermic on Vo-SBTO.

The variation of the N-N bond length was also monitored by the $*N_2$ protonation model on Vo-SBTO (Figure 5b), in the order of free N_2 molecule (1.078 Å) < $*N_2$ (1.155 Å) < *N−NH (1.253 Å) < *N−NH_2 (1.290 Å) < *N−NH_3 (1.448 Å). The elongation of the N-N bond length signifies the activation of N_2 molecules by oxygen vacancies. From the electron density (ED) and electron density difference (EDD) profiles, one can see that when N_2 molecules are physically adsorbed on the pristine SBTO surface, electrons are transferred to the N_2 molecules (Figure 5c), and no electron transfer of Ti, O, Bi, and other atoms was found in the subsequent hydrogenation steps (Figure S42, Supporting Information), indicating that these electrons may come from the separated photogenerated electrons. For Vo-SBTO, significant electron transfer and enrichment occurred between Ti−Vo and N_2 molecules (Ti−Vo−N=N bonding mechanism) (Figure 5e), consistent with the N-N bond length variation, indicating that Vo indeed plays a crucial role in N_2 activation. In addition, during the hydrogenation of N_2 molecules, some electron loss was found in the O atoms around Ti, likely due to electron transfer from O to Vo through Ti.

The effect of different adsorption modes of N_2 molecules on the material surface on N_2 activation was then studied by analysis of the partial density of states (PDOS). For pristine SBTO (Figure 5f; Figure S43, Supporting Information), N_2 molecules are mainly physisorbed on the surface, and the only way to obtain electrons is from photogenerated electrons separated by the ferroelectric polarization field, where the low concentration greatly limits the activation of N_2. For Vo-SBTO (Figure 5g), the electron transfer between N_2 molecules and surface oxygen

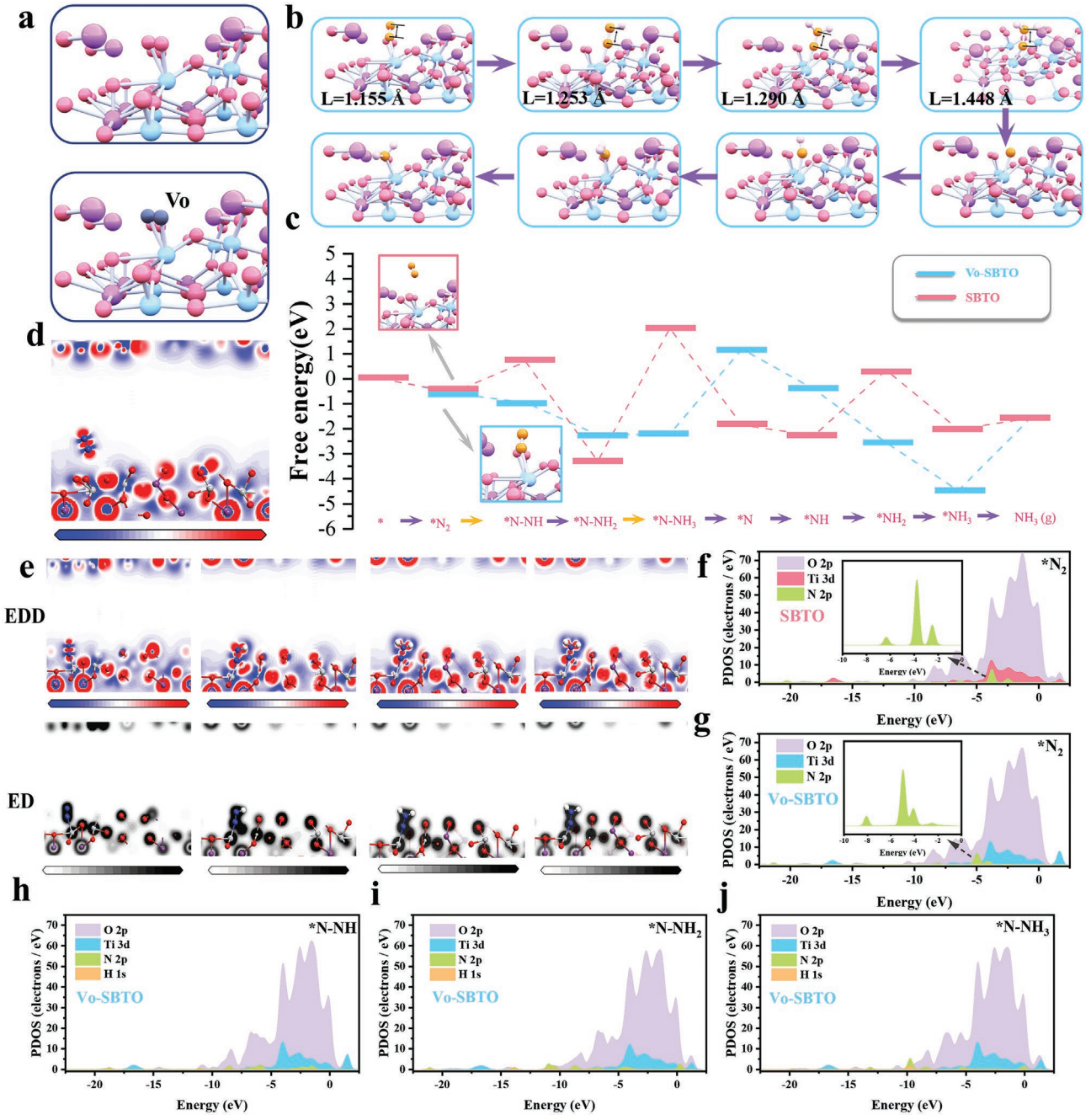

Figure 5. a) Pristine SBTO (top) and Vo-SBTO models (bottom) for DFT theoretical calculations. b) Model schematic diagrams and c) Gibbs free energy diagrams of intermediates generated during N_2-to-NH_3 catalysis on pristine SBTO and Vo-SBTO. d) Electron density difference (EDD) of N_2 molecules adsorbed on a pristine SBTO surface, where red represents electron gain and blue represents electron loss. e) Electron density (ED) and EDD of N_2 molecule protonation ($*N_2 \rightarrow *N{-}NH_3$) during photocatalyzed synthesis of NH_3 by Vo-SBTO, where red represents electron gain and blue represents electron loss. PDOS of N_2 molecules are adsorbed on f) pristine SBTO and g) Vo-SBTO. h–j) PDOS of the N_2 molecule protonation process ($*N{-}NH \rightarrow *N{-}NH_3$) on the surface of Vo-SBTO.

vacancies results in full crossover, leading to strong broadening and splitting of the N 2p orbitals with the surface Ti 3d and O 2p electronic states. The maximal interaction of the N_2 molecules with the surface oxygen vacancies facilitates the transfer of photogenerated electrons from Ti—Vo to the π^* antibonding orbital (lowest unoccupied molecular orbital) of molecular N_2; and hence, N_2 activation and subsequent protonation.[44a,45] Compared with physisorption, chemisorbed N_2 molecules are more likely to acquire electrons. During the subsequent protonation process ($*N{-}NH \rightarrow *N{-}NH_3$), the electronic states of O 2p gradually decrease, and the N 2p orbital continues to split and maintain sufficient overlap with the H 1s orbital (Figure 5h–j; Figure S44, Supporting Information). This confirms that the O atoms attached to Ti inject electrons into Vo

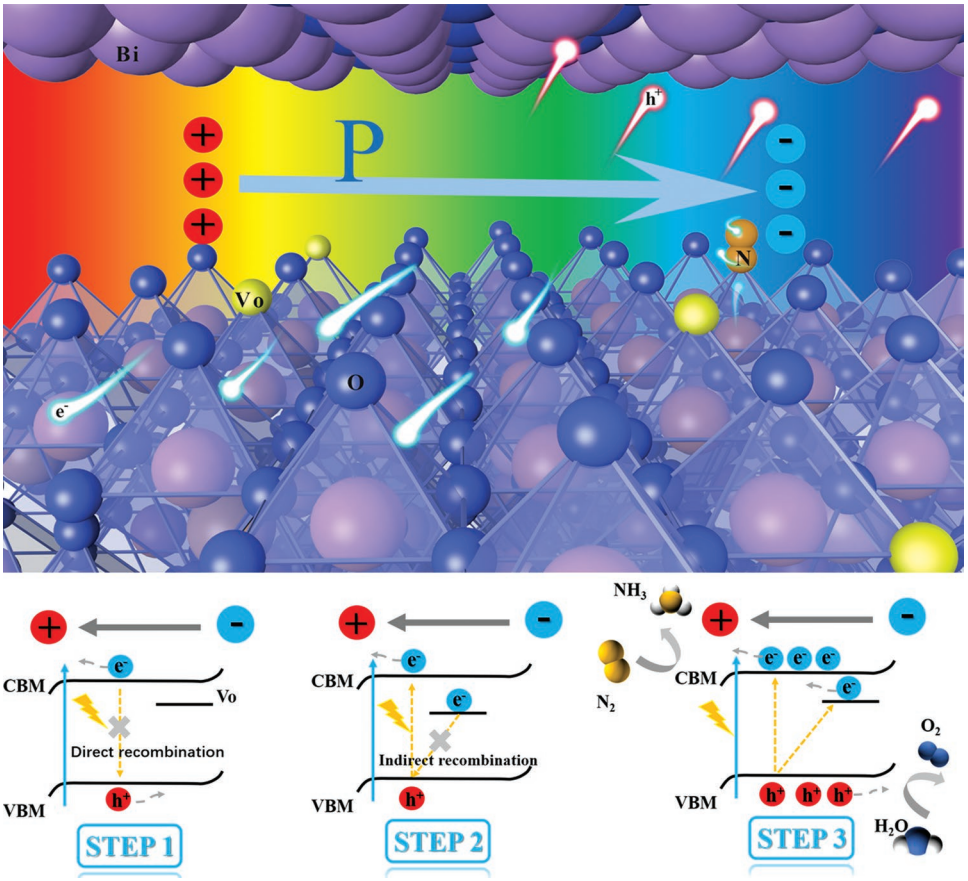

Figure 6. Schematic illustration of the synergistic enhancement of interfacial electron transfer process by oxygen vacancies and ferroelectric polarization fields.

to keep the N_2 molecules continuously activated. Therefore, it is believed that the introduction of oxygen vacancies enables the formation of three electron-transfer pathways on Vo-SBTO for N_2 activation: a) upon photoexcitation, the photogenerated electrons migrate to the surface of the material due to the ferroelectric polarization field; b) the photogenerated electrons are directly captured by oxygen vacancies and efficiently transferred to the vacant antibonding orbitals of adsorbed N_2; and c) O atoms around Ti inject electrons into N_2 molecules through the Ti—Vo pathway (O—Ti—Vo—N=N). This means that oxygen vacancies can not only greatly enhance the adsorption of N_2 but also facilitate the subsequent protonation of N_2 molecules into NH_3.

With the combined experimental and DFT results, the enhanced photocatalytic activity of Vo-SBTO can be ascribed to the following factors: a) oxygen vacancies greatly enhance the photo absorption of SBTO in the visible range and increase the concentration of photoexcited carriers, b) oxygen vacancies enhance N_2 chemisorption and activation, c) oxygen vacancies accentuate the buildup of polarized charges at the opposite ends of the nanosheets that bend the energy band and the accompanying IEF due to the asymmetric center of SBTO, and d) due to surface defects, the SBTO becomes increasingly hydrophilic and exhibits enhanced contact with water and dissolved nitrogen in the water.

The synergistic effect of ferroelectric polarization and oxygen vacancies in facilitating N_2 fixation to NH_3 can be summarized in **Figure 6**. Under photoirradiation, the photogenerated electrons are transferred to the $[TiO_6]$ layer and migrate from the interior to the surface active sites. For Vo-SBTO, such charge migration can be boosted by the ferroelectric polarization field parallel to the $[Bi_2O_2]^{2+}$ layer. Meanwhile, oxygen vacancies can act as electrons traps in the CB, effectively transferring the captured electrons to the empty π antibonding orbitals of the adsorbed N_2 (Figure S45, Supporting Information). During the hydrogenation of N_2, the electron transfer path of O—Ti—Vo—N=N is found to be conducive to N_2 protonation. The direct and indirect recombination of photogenerated carriers is effectively inhibited under the synergistic effect of oxygen vacancies and ferroelectric polarization field, leading to an increase of the concentration of charge carriers that can reach the surface for redox reactions.

Notably, whereas oxygen vacancies working in concert with ferroelectricity are beneficial for SBTO photocatalysis, too high a concentration of oxygen vacancies can disrupt the ferroelectric structure,[46] lead to excessive trapping of photogenerated carriers, and impede migration to the catalyst surface; and hence, compromise the eventual photocatalytic performance.[25] SBTO-2 represents the optimal catalyst within the present experimental context.

3. Conclusion

Self-polarized ferroelectric SBTO nanosheets were prepared by a facile hydrothermal procedure. A second hydrothermal treatment in the presence of glyoxal as the reducing agent led to the generation of oxygen vacancies. Among the series of samples, SBTO-2 showed the best N_2 activation and NH_3 production efficiency of 53.41 μmol g^{-1} h^{-1} under simulated solar light. The combined results from experimental and theoretical studies demonstrated that the oxygen vacancies and the IEF generated by self-polarization synergistically extended the photo absorption to the visible range, improved the charge separation efficiency, and facilitated the chemisorption and activation of N_2 molecules. Results from this study highlight the unique potential of structural engineering of ferroelectric materials in the development of high-performance photocatalysts for nitrogen fixation to ammonia.

Supporting Information

Supporting Information is available from the Wiley Online Library or from the author.

Acknowledgements

This work was supported by the Natural Science Foundation of China (NSFC, 21471103 and 52100069). S.W.C. thanks the US National Science Foundation (CBET-1848841 and CHE-1900235) for partial support of the work.

Conflict of Interest

The authors declare no conflict of interest.

Data Availability Statement

The data that support the findings of this study are available from the corresponding author upon reasonable request.

Keywords

charge separation, ferroelectric polarization, nitrogen adsorption, oxygen vacancy, photocatalytic nitrogen fixation

Received: October 5, 2022
Revised: November 4, 2022
Published online: November 22, 2022

[1] a) Y. Chen, C. Zhao, S. Ma, P. Xing, X. Hu, Y. Wu, Y. He, *Inorg. Chem. Front.* **2019**, *6*, 3083; b) C. Xiao, H. Wang, L. Zhang, S. Sun, W. Wang, *ChemCatChem* **2019**, *11*, 6467; c) Q. Zhu, Q. Xu, M. Du, X. Zeng, G. Zhong, B. Qiu, J. Zhang, *Adv. Mater.* **2022**, *34*, 2202929; d) N. Zhang, A. Jalil, D. Wu, S. Chen, Y. Liu, C. Gao, W. Ye, Z. Qi, H. Ju, C. Wang, X. Wu, L. Song, J. Zhu, Y. Xiong, *J. Am. Chem. Soc.* **2018**, *140*, 9434.

[2] a) X. Gao, Y. Shang, L. Liu, F. Fu, *J. Catal.* **2019**, *371*, 71; b) H. Liu, P. Wu, H. Li, Z. Chen, L. Wang, X. Zeng, Y. Zhu, Y. Jiang, X. Liao, B. S. Haynes, J. Ye, C. Stampfl, J. Huang, *Appl. Catal. B* **2019**, *259*, 118026.

[3] a) C. Zhao, Y. Li, H. Chu, X. Pan, L. Ling, P. Wang, H. Fu, C.-C. Wang, Z. Wang, *J. Hazard. Mater.* **2021**, *419*, 126466; b) S. Wang, X. Hai, X. Ding, K. Chang, Y. Xiang, X. Meng, Z. Yang, H. Chen, J. Ye, *Adv. Mater.* **2017**, *29*, 1701774.

[4] a) A. J. Medford, M. C. Hatzell, *ACS Catal.* **2017**, *7*, 2624; b) R. F. Service, *Science* **2018**, *361*, 120; c) H. Hirakawa, M. Hashimoto, Y. Shiraishi, T. Hirai, *J. Am. Chem. Soc.* **2017**, *139*, 10929; d) Y. Zhao, Y. Zhao, R. Shi, B. Wang, G. I. N. Waterhouse, L.-Z. Wu, C.-H. Tung, T. Zhang, *Adv. Mater.* **2019**, *31*, 1806482; e) Y. Liu, M. Cheng, Z. He, B. Gu, C. Xiao, T. Zhou, Z. Guo, J. Liu, H. He, B. Ye, B. Pan, Y. Xie, *Angew. Chem., Int. Ed.* **2019**, *58*, 731.

[5] a) J. Yang, H. Bai, Y. Guo, H. Zhang, R. Jiang, B. Yang, J. Wang, J. C. Yu, *Angew. Chem., Int. Ed.* **2021**, *60*, 927; b) J. Yang, Y. Guo, R. Jiang, F. Qin, H. Zhang, W. Lu, J. Wang, J. C. Yu, *J. Am. Chem. Soc.* **2018**, *140*, 8497; c) C. Li, T. Wang, Z.-J. Zhao, W. Yang, J.-F. Li, A. Li, Z. Yang, G. A. Ozin, J. Gong, *Angew. Chem., Int. Ed.* **2018**, *57*, 5278; d) Y. Wu, H. Ji, Q. Liu, Z. Sun, P. Li, P. Ding, M. Guo, X. Yi, W. Xu, C.-C. Wang, S. Gao, Q. Wang, W. Liu, S. Chen, *J. Hazard. Mater.* **2022**, *424*, 127563.

[6] a) P. Ding, H. Ji, P. Li, Q. Liu, Y. Wu, M. Guo, Z. Zhou, S. Gao, W. Xu, W. Liu, Q. Wang, S. Chen, *Appl. Catal., B* **2022**, *300*, 120633; b) J. Y. Y. Loh, G. Sharma, N. P. Kherani, G. A. Ozin, *Adv. Energy Mater.* **2021**, *11*, 2101566; c) P. Yang, R. Zhao, J. Liu, T. Wang, C. Feng, H. Hu, G. Xue, *Adv. Mater. Interfaces* **2022**, *9*, 2102031; d) J. Li, X. Li, S. Yu, S. Gao, Y. Zhang, Y. Li, C. Wang, Q. Wang, *Chin. Chem. Lett.* **2022**, https://doi.org/10.1016/j.cclet.2022.04.015.

[7] a) H. Maimaitizi, A. Abulizi, T. Zhang, K. Okitsu, J.-J. Zhu, *Ultrason. Sonochem.* **2020**, *63*, 104956; b) L. Pan, S. Sun, Y. Chen, P. Wang, J. Wang, X. Zhang, J.-J. Zou, Z. L. Wang, *Adv. Energy Mater.* **2020**, *10*, 2000214; c) X. Li, W. Wang, F. Dong, Z. Zhang, L. Han, X. Luo, J. Huang, Z. Feng, Z. Chen, G. Jia, T. Zhang, *ACS Catal.* **2021**, *11*, 4739; d) C. Hu, S. Tu, N. Tian, T. Ma, Y. Zhang, H. Huang, *Angew. Chem., Int. Ed.* **2021**, *60*, 16309.

[8] H. Zheng, X. Li, K. Zhu, P. Liang, M. Wu, Y. Rao, R. Jian, F. Shi, J. Wang, K. Yan, J. Liu, *Nano Energy* **2022**, *93*, 106831.

[9] H. Yu, F. Chen, X. Li, H. Huang, Q. Zhang, S. Su, K. Wang, E. Mao, B. Mei, G. Mul, T. Ma, Y. Zhang, *Nat. Commun.* **2021**, *12*, 4594.

[10] C. Wang, F. Chen, C. Hu, T. Ma, Y. Zhang, H. Huang, *Chem. Eng. J.* **2022**, *431*, 133930.

[11] J. Zhu, X.-B. Chen, J.-h. He, J.-C. Shen, *Phys. Lett. A* **2007**, *362*, 471.

[12] Q. Zhu, A. A. Dar, Y. Zhou, K. Zhang, J. Qin, B. Pan, J. Lin, A. O. T. Patrocinio, C. Wang, *ACS ES&T Engg* **2022**, *2*, 1365.

[13] S. Tu, Y. Zhang, A. H. Reshak, S. Auluck, L. Ye, X. Han, T. Ma, H. Huang, *Nano Energy* **2019**, *56*, 840.

[14] a) M. Ai, J.-W. Zhang, Y.-W. Wu, L. Pan, C. Shi, J.-J. Zou, *Chem Asian J* **2020**, *15*, 3599; b) N. Zhang, C. Gao, Y. Xiong, *J Energy Chem* **2019**, *37*, 43.

[15] J. Xiong, P. Song, J. Di, H. Li, *Chem. Eng. J.* **2020**, *402*, 126208.

[16] P. Li, Z. Zhou, Q. Wang, M. Guo, S. Chen, J. Low, R. Long, W. Liu, P. Ding, Y. Wu, Y. Xiong, *J. Am. Chem. Soc.* **2020**, *142*, 12430.

[17] a) R. Su, Z. Wang, L. Zhu, Y. Pan, D. Zhang, H. Wen, Z.-D. Luo, L. Li, F.-T. Li, M. Wu, L. He, P. Sharma, J. Seidel, *Angew. Chem., Int. Ed.* **2021**, *60*, 16019; b) L. Liu, H. Huang, F. Chen, H. Yu, N. Tian, Y. Zhang, T. Zhang, *Sci. Bull.* **2020**, *65*, 934.

[18] a) S. Yu, Y. Zhang, F. Dong, M. Li, T. Zhang, H. Huang, *Appl. Catal., B* **2018**, *226*, 441; b) H. Yu, J. Li, Y. Zhang, S. Yang, K. Han, F. Dong, T. Ma, H. Huang, *Angew. Chem., Int. Ed.* **2019**, *58*, 3880.

[19] C. H. Hervoches, A. Snedden, R. Riggs, S. H. Kilcoyne, P. Manuel, P. Lightfoot, *J. Solid State Chem.* **2002**, *164*, 280.

[20] a) Y. L. Du, G. Chen, M. S. Zhang, *Solid State Commun.* **2004**, *132*, 175; b) Z. Zhang, X. Li, Z. Huang, L. Zhang, J. Han, X. Zhou, D. Guo, Y. Ju, *J. Mater. Sci.: Mater. Electron.* **2018**, *29*, 7453.
[21] a) T. Cheng, H. Gao, X. Sun, T. Xian, S. Wang, Z. Yi, G. Liu, X. Wang, H. Yang, *Adv. Powder Technol.* **2021**, *32*, 951; b) C. Zhang, Y. Wang, X. Zhang, R. Wang, L. Kou, J. Wang, R. Li, C. Fan, *Chem. Eng. J.* **2021**, *417*, 128218.
[22] a) Z. Xie, X. Tang, J. Shi, Y. Wang, G. Yuan, J.-M. Liu, *Nano Energy* **2022**, *98*, 107247; b) X. Wang, Y. Wang, M. Gao, J. Shen, X. Pu, Z. Zhang, H. Lin, X. Wang, *Appl. Catal. B* **2020**, *270*, 118876.
[23] Y. Zhu, W. Zhou, J. Sunarso, Y. Zhong, Z. Shao, *Adv. Funct. Mater.* **2016**, *26*, 5862.
[24] H. Yu, H. Huang, K. Xu, W. Hao, Y. Guo, S. Wang, X. Shen, S. Pan, Y. Zhang, *ACS Sustainable Chem. Eng.* **2017**, *5*, 10499.
[25] H. Li, J. Shang, Z. Ai, L. Zhang, *J. Am. Chem. Soc.* **2015**, *137*, 6393.
[26] a) M. Tan, Y. Ma, C. Yu, Q. Luan, J. Li, C. Liu, W. Dong, Y. Su, L. Qiao, L. Gao, Q. Lu, Y. Bai, *Adv. Funct. Mater.* **2022**, *32*, 2111740; b) N. Li, Y. Zhu, F. Jiao, X. Pan, Q. Jiang, J. Cai, Y. Li, W. Tong, C. Xu, S. Qu, B. Bai, D. Miao, Z. Liu, X. Bao, *Nat. Commun.* **2022**, *13*, 2742; c) D. Cui, K. Xu, X. Dong, D. Lv, F. Dong, W. Hao, Y. Du, J. Chen, *Commun Chem* **2020**, *3*, 73.
[27] Q. Han, X. Bai, J. Chen, S. Feng, W. Gao, W. Tu, X. Wang, J. Wang, B. Jia, Q. Shen, Y. Zhou, Z. Zou, *Adv. Mater.* **2021**, *33*, 2006780.
[28] Z. Zhao, D. Wang, R. Gao, G. Wen, M. Feng, G. Song, J. Zhu, D. Luo, H. Tan, X. Ge, W. Zhang, Y. Zhang, L. Zheng, H. Li, Z. Chen, *Angew. Chem., Int. Ed.* **2021**, *60*, 11910.
[29] a) Y. Zhao, R. Shi, X. Bian, C. Zhou, Y. Zhao, S. Zhang, F. Wu, G. I. N. Waterhouse, L.-Z. Wu, C.-H. Tung, T. Zhang, *Adv. Sci.* **2019**, *6*, 1802109; b) Y. Zhao, F. Wu, Y. Miao, C. Zhou, N. Xu, R. Shi, L.-Z. Wu, J. Tang, T. Zhang, *Angew. Chem., Int. Ed.* **2021**, *60*, 21728.
[30] L. Li, J. Yan, T. Wang, Z.-J. Zhao, J. Zhang, J. Gong, N. Guan, *Nat. Commun.* **2015**, *6*, 5881.
[31] Y. Lin, Y. Zhang, C. Sun, S. Zhan, Q. Yuan, H. Yang, *Ceram. Int.* **2020**, *46*, 15270.
[32] a) W. Zhang, G. Pan, D. Han, T. Liu, W. Liang, D. Han, M. Dai, H. Xie, D. Qin, L. Niu, *Res. Square.* **2022**, https://doi.org/10.21203/rs.3.rs-1614980/v1; b) L. Bao, Q. Bao, H. Zhang, Y. Yuan, *ChemPhysChem* **2021**, *22*, 2168.
[33] a) T. Wang, C. Feng, J. Liu, D. Wang, H. Hu, J. Hu, Z. Chen, G. Xue, *Chem. Eng. J.* **2021**, *414*, 128827; b) Y. Zhang, J. Di, X. Qian, M. Ji, Z. Tian, L. Ye, J. Zhao, S. Yin, H. Li, J. Xia, *Appl. Catal., B* **2021**, *299*, 120680.
[34] G. Li, F. Li, J. Liu, C. Fan, *J. Solid State Chem.* **2020**, *285*, 121245.
[35] a) Z. Zhao, D. Yang, H. Ren, K. An, Y. Chen, Z. Zhou, W. Wang, Z. Jiang, *Chem. Eng. J.* **2020**, *400*, 125929; b) L. Deng, L. Wang, G. Wei, H. Yuan, J. Xie, Y. Chen, *Electrochim. Acta* **2022**, *408*, 139934; c) Y. Shen, J. Shou, L. Chen, W. Han, L. Zhang, Y. Chen, X. Tu, S. Zhang, Q. Sun, Y. Chang, H. Zheng, *Appl. Catal., A* **2022**, *643*, 118739.
[36] a) L. Liu, H. Huang, Z. Chen, H. Yu, K. Wang, J. Huang, H. Yu, Y. Zhang, *Angew. Chem., Int. Ed.* **2021**, *60*, 18303; b) M. Guo, G. Tan, W. Yang, L. Lv, Z. Yue, Z. Chai, Y. Liu, H. Ren, A. Xia, R. Tan, *J. Alloys Compd.* **2018**, *741*, 420; c) P. Niu, Z. Zhang, F. Wang, K. Yan, *Ceram. Int.* **2021**, *47*, 30439.
[37] a) C. Hu, J. Hu, Z. Zhu, Y. Lu, S. Chu, T. Ma, Y. Zhang, H. Huang, *Angew. Chem., Int. Ed.* **2022**, https://doi.org/10.1002/anie.202212397; b) F. Wang, J. Zhang, C.-C. Jin, X. Ke, F. Wang, D. Liu, *Nano Energy* **2022**, *101*, 107573.
[38] X. Fan, Z. Wu, L. Wang, C. Wang, *Chem. Mater.* **2017**, *29*, 639.
[39] B. Liao, X. Liao, H. Xie, Y. Qin, Y. Zhu, Y. Yu, S. Hou, Y. Zhang, X. Fan, *J. Mater. Sci. Technol.* **2022**, *123*, 222.
[40] M. Li, S. Yu, H. Huang, X. Li, Y. Feng, C. Wang, Y. Wang, T. Ma, L. Guo, Y. Zhang, *Angew. Chem., Int. Ed.* **2019**, *58*, 9517.
[41] Y. Huang, N. Zhang, Z. Wu, X. Xie, *J. Mater. Chem. A* **2020**, *8*, 4978.
[42] M. Li, H. Huang, J. Low, C. Gao, R. Long, Y. Xiong, *Small Methods* **2019**, *3*, 1800388.
[43] X. a. Dong, Z. Cui, X. Shi, P. Yan, Z. Wang, A. C. Co, F. Dong, *Angew. Chem., Int. Ed.* **2022**, *61*, e202200937.
[44] a) Y. Gu, B. Xi, W. Tian, H. Zhang, Q. Fu, S. Xiong, *Adv. Mater.* **2021**, *33*, 2100429; b) E. Skúlason, T. Bligaard, S. Gudmundsdóttir, F. Studt, J. Rossmeisl, F. Abild-Pedersen, T. Vegge, H. Jónsson, J. K. Nørskov, *Phys. Chem. Chem. Phys.* **2012**, *14*, 1235.
[45] J. M. G. Vilar, G. Gomila, J. M. Rubí, *Phys. Rev. Lett.* **1998**, *81*, 14.
[46] D. R. Islamov, T. V. Perevalov, *Microelectron. Eng.* **2019**, *216*, 111041.